Content type: Article

Hetero-Integration of Silicon Nanomembranes with 2D Materials for Transient, Bioresorbable Neurochemical System

Seung Min Yang[1], Jae Hyung Shim[1], Hyun-U Cho[2], Tae-Min Jang[1], Gwan-Jin Ko[1], Jeongeun Shim[2], Tae Hee Kim[3], Jia Zhu[5], Sangun Park[3,4], Yoon Seok Kim[1], Su-Yeon Joung[1], Jong Chan Choe[1], Jeong-Woong Shin[1], Joong Hoon Lee[1], Yu Min Kang[2], Huanyu Cheng[5], Youngmee Jung[3,6,7], Chul-Ho Lee[1]*, Dong Pyo Jang[2]* and Suk-Won Hwang[1]*

Correspondence: Chul-Ho Lee (chlee80@korea.ac.kr), Dong Pyo Jang (dongpjang@hanyang.ac.kr), or Suk-Won Hwang (dupong76@korea.ac.kr)

[1] KU-KIST Graduate School of Converging Science and Technology, Korea University, 145 Anam-ro, Seongbuk-gu, Seoul, 02841, Republic of Korea

[2] Department of Biomedical Engineering, Hanyang University, 222, Wangsimni-ro, Seongdong-gu, Seoul, 04763, Republic of Korea

[3] Center for Biomaterials, Biomedical Research Institute, Korea Institute of Science and Technology (KIST), Seoul, 02792, Republic of Korea

[4] Institute of Animal Molecular Biotechnology and Department of Biotechnology, College of Life Sciences and Biotechnology, Korea University, 145, Anam-ro, Seongbuk-gu, Seoul, 02841, Republic of Korea

[5] Department of Engineering Science and Mechanics, The Pennsylvania State University, University Park, Pennsylvania, 16802, USA

[6] School of Electrical and Electronic Engineering, Yonsei University, Seoul, 03722, Republic of Korea

[7] Yonsei-KIST Convergence Research Institute, Seoul, 03722, Republic of Korea

These authors contributed equally: Seung Min Yang, Jae Hyung Shim, Hyun-U Cho

Keywords: bioresorbable, transient, 2D materials, silicon nanomembranes, neurochemical

ABSRACT

Although neurotransmitters are key substances closely related to evaluate degenerative brain diseases as well as regulate essential functions in the body, many research efforts have been focused on monitoring relatively associated physical, mechanical and electrophysiological parameters, rather than direct observation of such biochemical messengers. Here, we introduce a soft, bioresorbable silicon-based neurochemical analyzer incorporated with two-dimensional transition metal dichalcogenides as a completely implantable brain-hacking system that can collect time-dynamic behaviors of dopamine and relevant parameters in peripheral regions at the same time. Extensive range of examinations of molybdenum/tungsten disulfide (MoS_2/WS_2) nanosheets and catalytic iron nanoparticles (Fe NPs) highlights underlying mechanisms of strong chemical and target-specific responses to the neurotransmitters along with theoretical modeling tools. Systematic characterizations demonstrate reversible, stable and long-term operational performances of the degradable bioelectronics with excellent sensitivity and selectivity over those of non-dissolvable counterparts. A complete set of in vivo experiments with comparative analysis using carbon fiber electrodes illustrates capabilities for a potential use as a clinically accessible tool to associated neurodegenerative diseases.

INTRODUCTION

Improved life expectancy has been accompanied by a noticeable increase in diverse types of age-related diseases – ranging from cardiovascular disease, and Parkinson's and Alzheimer's disease related to the brain and heart as key organs, to cancer and diabetes – that are more likely to occur in the elderly over the age of 60. Exampled approaches attempting to prevent, treat and manage those diseases and other symptoms include techniques or tools such as electroencephalography (EEG), electrocardiography (ECG), fingerprick blood sugar meter and insulin pumps as a non-invasive or minimally-invasive form, while electrocorticography (ECoG), microelectrode arrays (MEAs), deep brain stimulator (DBS), coronary angioplasty and stents, and pacemakers as an invasive procedure.[1–9] Despite those well-established technologies that can provide accurate and reliable information with practical benefits to clinical medicine, a strong desire to efficiently couple with the human body motivated developments of technologies in the context of a platform for soft, light-weight and miniaturized, as well as biologically benign and bioresorbable electronics. Such progress resulted in epidermal or skin-like electronics[10–14], self-healing components[15,16], optogenetics[17,18], passive/active drug delivery systems[19–21] and transient/biodegradable electronics[22–25], as parts of wearable and implantable electronic systems. While most interests for early diagnosis or observation of diseases using these various techniques have largely relied on physical, mechanical or electrical parameters[21,24,26–28], chemical or biochemical factors have been relatively less considered for study or limited to fast-scan cyclic voltammetry (FSCV) using carbon fiber-based electrodes that are typically not a completely implantable and bioresorbable form.[29–31]

New materials design and/or heterogeneous integration of multiple elements can be a useful strategy to suggest a key to the settlement of current hurdles particularly in realizing a fully implantable, bioresorbable system that can monitor chemical or biochemical

information. In this respect, the use of atomically thin transition metal dichalcogenides (TMDs) combined with existing, conventional components might provide an unprecedented opportunity to explore potential research fields due to their attractive characteristics, including mechanical flexibility, robustness, low-cost synthesis, electrical/optical tunability and catalytic activity.[32–42] In particular, chemical manipulation (e.g., layer-by-layer exfoliation, charge transfer doping and surface/edge functionalization) allows for modifying properties of TMDs in a desired way to create or tailor versatile features such as biodegradability and electrical/electrochemical performance through engineering of atomic defects or structural phases.[43–48]

In the following, we present a soft, bioresorbable silicon-based brain-hacking system capable of monitoring neurochemical messengers and peripheral neurophysiologies (pH, temperature and electrophysiology), with a fully implantable format that allows minimally invasive penetration into a deep brain region. A solution-processable heterostructure of two-dimensional (2D) TMDs (MoS_2 and WS_2) and iron (Fe) nanoparticles provides a dissolvable electrochemical platform for detecting changes in a range of concentration of a neurotransmitter (i.e. dopamine) that is closely relevant to neurological disorders, with exceptional sensitivity, selectivity, and reversible and stable operations. In vivo investigations demonstrate functionalities of the precise, multimodal and real-time biochemical analyzer as system-level feasibilities.

RESULTS

Biodegradable Electronic System with Versatile Functions for Transient Deep Brain Monitors

Figure 1a illustrates an exploded view of soft, non-toxic, bioresorbable electronic brain-hacking system in a thin, narrow and tapering geometry, designed to investigate and

obtain information on neurochemicals and neurophysiologies in selective deep brain regions. The exploratory probe was systematically built with several essential components: i) electrochemical device as a primary element consisted of monocrystalline silicon nanoribbons (NRs, thickness ~300 nm) uniformly coated with a multi-dimensional heterostructure of two-dimensional transition metal dichalcogenide (2D TMD) nanosheets and iron nanoparticles (Fe NPs), capable of detecting neurotransmitters with high sensitivity and selectivity over other chemical substances; ii) Peripheral electronic constituents such as pH meters, temperature sensors and electrophysiological (EP) electrodes, were assembled to analyze the correlation via simultaneously monitoring variations of diverse parameters along with the release of neurotransmitters in a broad scientific sense; iii) Wireless communication system installed outside the brain was connected to the hacking probe to transmit the measured vital signals for ultimate free movements. Details on materials preparation and devices fabrication appeared in methods and supplementary information. Figures 1b and S1 present an overall system configuration highlighted with a mechanically deformable feature using a brain phantom and other tools, with an enlarged view of the key region of the system in the inset. Figure 1c illustrates the overall mechanism by which dopamine, as a neurotransmitter, is transduced into electrical signals through electrostatic interactions with the electrochemical system. The bioresorbable hybrid component consists of three essential materials: i) p-doped silicon nanomembranes (p-Si NMs); ii) metallic 1T-phase TMD nanosheets dispersed on the p-Si NMs; and iii) catalytic Fe nanoparticles (Fe NPs) decorated on the TMD nanosheets. Here, the positively charged dopamine (DA) is strongly attracted to the negatively charged TMD-Fe NPs surface by electrostatic interaction, increasing the probability that the Fe-NPs as a catalytic converter oxidize DA to dopamine quinone (DQ). The electrons generated by DA oxidation are then transferred to the semiconducting Si NMs through the ultrathin, highly conductive TMDs, leading to changes in electrical signals

according to concentrations of dopamine. In this context, a strong negative electrostatic potential of the TMD-Fe NPs for dopamine adsorption, a large number of Fe NPs catalysts for dopamine oxidation, and a pure 1T-TMDs ratio for efficient electron transfer, are particularly important for highly sensitive detection of DA, which have been thoroughly investigated in the following experiments. All of the electronic elements as well as the constituent materials can be completely dissolved via hydrolysis over time as described in Figure S2 while semi-submerged in an artificial biological solution with electrolytes concentration (127 mM NaCl, 1.0 mM KCl, 1.2 mM KH_2PO_4, 26 mM $NaHCO_3$, 10 mM D-glucose, 2.4 mM $CaCl_2$, 1.3 mM $MgCl_2$), oxygen level (95 % O_2, 5 % CO_2), and osmolarity (~ 300 mOsm) that matched to cerebrospinal fluid in the central nervous system.[49] Dissolution property and chemistry of constituent elements was summarized in supplementary Table 1. Figure 1d presents dissolution behaviors of patterned nanosheets of MoS_2 (top) and WS_2 (bottom) during immersion in a buffer solution (0.1 M, pH 11) at 60 ^oC, whose dissolution mechanisms and associated evaluations are described in detail in a subsequent paragraph.

Engineering of Two-Dimensional Nano TMD materials combined with Catalyst NPs for Bioresorbable Electrochemical Platforms

Figure 2 presents the fundamental analysis in spectroscopic, catalytic, electrochemical characterizations of TMDs-Fe hybrids built as key recognition components of a degradable electrochemical system. Chemically exfoliated TMDs via lithium (Li) intercalation, as opposed to ones from chemical vapor deposition (CVD) or mechanical exfoliation, typically contain numerous active sites, such as edges and vacancies, which can bind to ligands or nanoparticles. Figure 2a shows transmission electron microscope (TEM) images of defect-rich TMDs uniformly decorated with Fe NPs especially at edges, which

motivated us to utilize flake-like nanosheets rather than large-scale, defect-free films. Raman spectra of lithium-intercalated TMDs in Figure 2b reveal the phase transition behavior from 2H-semiconducting to 1T-metallic phase depending on intercalation temperatures. Crystal structures of both phases appeared in Figure S3. In addition to typical peaks of E^1_{2g} at 383 (352) and A_{1g} at 410 (420) cm^{-1} of pristine 2H-MoS_2 (-WS_2) at room temperature (25 ^oC), a J_1 peak for MoS_2 at ~156 cm^{-1} – a characteristic of phase transition – was observed, while the corresponding peak for WS_2 (J_1) at 128 cm^{-1} did not appear despite its evolution at high temperatures. The result indicates that the phase transition of WS_2 required relatively higher driving energy than that of MoS_2, which were similarly acquired from X-ray photoelectron spectroscopy (XPS) and X-ray diffraction (XRD) analyses (Figure 2c, S4). As the temperature increased, proportional increments of the intensities of J_1 peaks were apparent. As processed at 130 ^oC, the J_1 peak became dominant over negligible E^1_{2g} and A_{1g} modes, revealing a complete conversion from the 2H to the 1T phase particularly for MoS_2. These results are in good agreement with gradual evolutions of Mo^{4+} $3d_{5/2}$ (W^{4+} $4f_{5/2}$) and Mo^{4+} $3d_{3/2}$ (W^{4+} $4f/_{7/2}$) peaks of 1T-MoS_2 (1T-WS_2) as presented in XPS spectra of Figure 2c. Given the XPS data, estimated portions of the metallic 1T phase increased up to 87 (60) % for MoS_2 (WS_2) (Figure 2d, black). Such contrast in the phase purity is mainly due to thermodynamic stability[50,51], which the phase-converted 1T-WS_2 turned out to be more stable than the MoS_2 counterpart (Figure S5). As the phase conversion proceeded, the stoichiometric composition ratio of sulfur and transition metal (Mo (W)) atoms varied from 2.0 for the pristine MoS_2 (WS_2) to ~1.6 (1.7) of the lithiated MoS_2 (WS_2) at 130 ^oC (Figure 2d, red). This S-deficient stoichiometry implies a significant generation of sulfur vacancies during Li intercalation, which offers anchoring sites for Fe NPs in the following steps. The high-purity metallic 1T-TMDs at 130 ^oC not only contain high electrical conductivity for efficient charge transfer but also provide a large number of active sites to attach Fe-NP

179 catalysts on the TMD surface.

180 The negative potential on the catalytic surface is critical to promote the adsorption of
181 positively charged neurotransmitters along with possessing high density catalytic sites.
182 Figure 2e shows measurements of ζ-potential at different stages in the process of hybridizing
183 the TMDs and Fe NPs. Sequential procedures and detailed analyses for integration of
184 TMDs with Fe NPs appeared in Figure S6-S10 and supplementary information. Although
185 the MPA ligand conjugation and Fe (III) reduction caused a slight shift toward positive values
186 of ζ-potential compared to ones of as-exfoliated nanosheets[45,52], the finalized hybrids of
187 MoS_2-Fe and WS_2-Fe still exhibited high negative ζ-potential (3 times more negative than ζ-
188 potential of reduced graphene oxide, rGO[53]), enabling to provide a favorable electrostatic
189 environment for dopamine adsorptions as well as stable colloidal dispersions.

190 Assessments of the resulting properties on catalytic performance were executed using
191 high-performance liquid chromatography (HPLC) whose the overall process involved
192 periodic samplings from a mixture (TMDs-Fe as a catalyst, DA as a target molecule to
193 oxidize, and deionized (DI) water as a solvent) at intervals of 15 minutes for an hour.
194 Measured absorbance signals at a wavelength of 280 nm in Figure 2f-g exhibited significant
195 decreases in DA at 11.3 min, whereas gradual increases in DQ at 13.2 min. Comparison of
196 such conversion rates estimated from areas of the peaks in the chromatograms suggested
197 effectiveness of the TMDs-Fe as a catalyst (Figures 2h and S11). Additional examinations
198 using analytical techniques such as FT-IR and H-NMR further confirmed the functional
199 groups and chemical structures of DQ molecules (Figure S12-13). Expected reaction
200 sequences of the conversion of DA into DQ appear in Figure S14.

201 Measured cyclic voltammograms (a scan rate of 100 mVs^{-1}) in Figures 2i and S15-17
202 ensured electrochemical activity of the complex catalytic products via investigation of the
203 reduction and oxidation procedures of DA (200 μM DA in PBS) using a commercial,

204 standard glassy carbon electrode (GCE, a working electrode, diameter ~3 mm) with Ag/AgCl
205 (a reference electrode) and a platinum (Pt) wire (a counter electrode). Both TMDs-Fe
206 coated GCEs exhibited obvious enhancements in anodic and cathodic current, particularly 4-
207 fold increase for the MoS_2-Fe compared to cases of a non-coated and TMDs-only GCEs,
208 which suggested the importance of a hybridized formation of constituent materials. Such
209 synergistic effects can be observed in electrochemical impedance measurements, which
210 promoted efficient transfer of the generated electrons to the underlying GCE through low
211 charge-transfer resistance (Figure S16). The overall results imply our design approach plays
212 a key role in enhancing both the catalytic activity and the electron transfer kinetics, which can
213 be verified by theoretical consideration with analytical modeling tools. As shown in Figure
214 2j-k, Fe atom at the surface of both 2H and 1T MoS_2 helped reduce the distance between
215 dopamine molecule and the MoS_2 layers due to increased bonding strength at the interface.
216 The existence of Fe atom on the surface of the 2H-MoS_2/dopamine reduced the distance from
217 3.98 Å to 2.66 Å, whereas it was reduced from 3.63 Å to 2.10 Å for the 1T-MoS_2/dopamine
218 system. The improved adsorption force can also be observed in the differential charge
219 density. In contrast to nearly no charge transfer at the MoS_2/dopamine interface (Figure 2j,
220 left for 2H and Figure 2k, left for 1T), the systems with the Fe atom exhibit electron transfers
221 from the dopamine to the MoS_2 slab as shown in the right frames of Figures 2j and 2k. The
222 most notable charge transfer observed in the 1T-MoS_2-Fe/dopamine system (Figure 2k, right)
223 highlights the best absorption at the MoS_2/dopamine interface among the studied systems.
224 This prediction was further verified by the calculated adsorption energies of the four different
225 systems (Figure 2l), which is also consistent with the experimental observations. The 1T-
226 MoS_2-Fe slab exhibited the highest absorption energy to the dopamine molecule (1.38 eV),
227 followed by the 2H-MoS_2-Fe slab (0.79 eV), the 1T-MoS_2 (0.10 eV), and then 2H-MoS_2
228 (0.04 eV). More details of the simulation work appear in supplementary information.

Detailed dissolution experiments via diverse tools were performed to study physical and chemical transient behaviors of the TMDs and blended components. Chemical reactions responsible for dissolution of the TMDs via hydrolysis are described in Figure 2m, where both cases form sulfate ions that can be verified by ion chromatography (IC) as shown in Figure 2n (left, PBS; right, ACSF). Gradual increases of the SO_4^{2-} ion over time revealed that the TMDs were dissolved in both aqueous solutions at physiological temperature (Figure 2o). Inspection of time-dependent behaviors of TMDs via changes in Raman signal were performed as a format of spatial mapping in the region of interest (J_1 mode) with corresponding spectra in a wide range of wavenumber (Figure S18). Complete degradation of these two 1T-TMD nanosheets occurred in ~ 4 weeks for MoS_2 and 8 weeks for WS_2, which is quite different from that of chemical-vapor-deposited 2H-MoS_2 monolayers in previous reports mainly due to the presence and extent of defects.[54] Between two materials, the relatively slow dissolution rate of WS_2 can be understood in a similar context of difficulty in inducing the phase transition in WS_2 compared to thermodynamically less stable MoS_2.

Characterizations of Flexible, Bioresorbable Sensor Systems for Neurochemicals and Neurophysiologies

Figure 3a corresponds to linear electrochemical responses of Si NRs decorated with synthesized MoS_2-Fe (red), WS_2-Fe (blue) to a wide range of dopamine concentrations (mM to fM) (details of device images and fabrication procedures appeared in Figure S19 and supplementary information). Predominant sensitive reactions of the Si/MoS_2-Fe electrodes over the Si/WS_2-Fe were derived from containing relatively a large fraction of the metallic 1T phase, enabling to efficiently convey more produced electrons to the Si transducers. Such excellent performance can be consistently accomplished even under continuous measurements in time domain during immersion in solutions of different concentrations

(Figure 3b). To assure durable, reliable capacity over a long period, we performed repeated tests with ~125 cycles through alternating two different concentrations of DA (1×10^{-12} M (pM), DA-free) in PBS (0.1 M) to observe variations of electrical signals. The bioresorbable chemical probes were able to retain more than 90 % of the initial value even after cyclic tests over 100 times (Si/WS_2-Fe) and 15 times (Si/MoS_2-Fe), and then gradually decayed in magnitude of 70 % near experiments of 120 (Si/WS_2-Fe) and 50 times (Si/MoS_2-Fe). Although the Si/MoS_2-Fe electrodes may be preferred over the Si/WS_2-Fe electrodes in terms of sensitivity, the latter provided stable, excellent performance in repetitive and long-term experiments, which can be enhanced or tuned through the phase engineering of the TMDs elements. Another key criterion for the validity of functional operations is to carefully evaluate dopamine-specific responses among other biochemical analytes including uric acid (UA), ascorbic acid (AA), serotonin (5-HT), epinephrine (EP), and norepinephrine (NE). As shown in Figure 3d, the ratios of selective reactions of both MoS_2-Fe (red) and WS_2-Fe (blue) were ~ 95 % and 92 % for UA, AA and 5-HT; ~ 80 % and ~60 % for EP and NE whose molecular structures are similar to that of DA, whereas negatively-charged silicon surface modified by hydroxyl groups provided no responses to all chemical messengers. Presumably, such selective capability could be attributed to the strong electrostatic interactions between the anionic TMDs and cationic DA since no chemical interactions were detected in the anion species (UA and AA) (Figure S20). Although 5-HT, EP and NE have positive electrostatic potentials induced by amine groups, steric hindrance in geometrical arrangement interferes with the electrostatic interactions. In addition, the relatively low oxidation potential of dopamine allows to perceive as being different from those positively charged molecules.[55] Similar outcomes were obtained in temporal measurements as negligible electrical changes occurred in the case of a dopamine-free buffer solution (PBS, 0.1 M), while appreciable variations arose in a dopamine-contained mixture (concentration, 1

279 nM) (Figure 3e).

280 Simultaneous view of changes in local physiological parameters involving pH,
281 temperature and electrophysiological signs associated with dopamine release enables
282 comprehensive, systematic analysis and interpretation for certain conditions. Figure 3f
283 shows measured changes in conductance of boron-doped (~ 10^{19} /cm^3) Si NRs-based pH
284 sensors, when exposed to solutions with a broad range of pH values. Complementary
285 functionalization of the Si NRs with hydroxy (-OH) and amino (-NH_2) groups improved
286 electrochemical responses via electrostatically induced charge depletion or accumulation in
287 the silicon channels associated with pH scales, resulting in the enhanced sensitivity of 1.25 ±
288 0.01 μS/pH superior to that of transient pH sensors in previously reported articles.[23] A
289 biologically useful thermometer can be achieved using a dissolvable passive conductor,
290 molybdenum (Mo), whose the temperature coefficient of resistance (α, ~ 0.0045 / C^o) is
291 comparable with that of platinum (Pt, ~ 0.0039 /C^o) as a commercial resistance temperature
292 detector (RTD).[56] Figure 3g exhibited linear characteristics of temperature-dependent
293 resistance of Mo-based RTD, the resulting sensitivity is ~0.26 % / ^{o}C, slightly lower than the
294 theoretical value. To verify the practical performance, we compared the responses with a
295 commercial component under external temperature modulation, and the accuracy of the
296 degradable Mo thermometer was nearly identical to that of a standard Pt-based sensor (Figure
297 3h). Electrical characteristics at interface between tissues and electrodes, which are closely
298 related to electrophysiological activity of the brain, were identified through electrochemical
299 impedance spectroscopy (EIS) under conditions similar to the environment in vivo (pH 7.4,
300 37 ^{o}C in PBS) using a hydrogel-based brain phantom. Figure 3i presents measured
301 distributions of amplitude (|Z|) and phase (θ) of individual Mo electrodes in a wide range of
302 frequencies, and the resulting behaviors were consistent with those published in the previous
303 researches or measured using a commercial electrode.[24] Measured data from the integrated

brain probes can be transmitted via wireless transmission, and detailed information of the RF system including image, protocol, and property appeared in Figure S21.

Deep Brain Examinations of Electrically Evoked and Pharmacologically Modulated Dopamine Release in Dorsal Striatum In Vivo Combined with Neurophysiological Monitoring

Figures 4a and S22-23 present surgical set-ups and coordination of electrodes for real-time efficacy of endoscopic deep brain observations. Bioresorbable brain-hacking systems were evaluated at the dorsomedial striatum through recording physiological changes (dopamine, pH, and temperature) in response to brief electrical stimulations of the medial forebrain bundle (MFB). At the same time, fast scan cyclic voltammetry (FSCV) was performed with a carbon fiber microelectrode (CFM) to identify optimal dopamine releasing sites in the dorsomedial striatum. Photograph in Figure 4b illustrates positions of each component (degradable probe, CFM, stimulation/reference electrodes) with a customized stereotactic frame, and a representative example of implanted neurochemical probes appeared in Figure S24. A slender stylus-like configuration with customized stereotactic frames (polylactic acid (PLA)) enabled the dissolvable bioelectronics to penetrate into the deep regions of the brain from cerebral cortex (approximate depth = 0 mm to 4 mm for rats) to nucleus accumbens (approximate depth = 9 mm for rats), with the ability to exquisitely address to the target depth with microscale control. Carbon fiber microelectrodes (CFM), whose adsorption properties have been well-recognized for dopamine researches[31], were employed as a guidance for cross-validation of DA signals, and stimulation electrodes were positioned at the medial forebrain bundle on the nigrostriatal pathway.

Color map in Figure 4c presents spatiotemporal mapping of released DA signals evoked by stimulations. Significant DA signals can be obtained as the brain probes were

329 reached into the target area connected to the stimulus of the MFB, which a reliable,
330 reproductive data set of electrically evoked phasic signals was accomplished by transient,
331 bioresorbable neural probes, in six biologically independent models (Figure 4d).
332 Measurements of individual models appeared in Figure S25 (the shades of grayscale denote
333 the extent of error bars). The temporal responses of the penetrated electronic probes sharply
334 increased and saturated during electrical stimulation, while they rapidly decreased to the
335 original state as the stimulation was removed. To confirm that the biological responses were
336 indeed produced by DA release via stimulations, we simultaneously performed electrical
337 collections using brain-hacking devices and CFM via fast-scan cyclic voltammetry (FSCV),
338 at a dorsal striatum about 5 mm beneath the surface of the rat brain. A representative color
339 map in Figure 4e exhibited significant current changes at 0.6 V/-0.2 V (DA
340 oxidation/reduction potential), demonstrating the resulting potentials were generated by the
341 excretion of dopamine. Time-variant current changes at DA oxidation potential indicated
342 the temporal response of DA oxidation was consistent with the one of the soft, degradable
343 neurochemical system (Figure 4f). Considering the estimated concentrations through
344 calibration, both techniques provided quite similar performance. Pharmacological treatment
345 can be a means to validate the capability for in vivo dopamine detection, via modulation of
346 extracellular dopamine concentrations. After dopamine is released by electric stimulus, the
347 dopamine transporter, DAT, rapidly reuptake dopamine from the extracellular space and
348 maintain equilibrium. Pharmacological inhibition of DAT with nomifensine as a dopamine
349 reuptake inhibitor has been utilized to provide enhanced phasic DA levels in extracellular
350 region.[57] Figure 4g presents collection of temporal changes in DA levels with stimulations
351 before/after intraperitoneal injection of nomifensine (20 mg/kg). Compared to dopamine
352 activities within the grayscale region (pre-drug administration), an apparent elevation of DA
353 signals was observed after the injection of nomifensine, indicating a double increase in the

354 average spike amplitude (left) and duration (right) summarized as normalized values in
355 Figure 4h. Raw data for an amplitude of peak currents and a half-life of phasic signals
356 appeared in Figure S26. Experiments using carbon microelectrodes-based FSCV provided
357 similar profiles and performances in Figure S27a-b. Observations in physiological signs in
358 conjunction with the release of dopamine can be an important part of a systematic
359 neurochemical monitor. Figure 4i shows the result of tracking variations of pH using
360 resorbable devices over time after stimulations. Such subtle changes in relatively long
361 period of time could be associated with neural activities including HCO^{3-} ion transport and a
362 rise of oxygen levels[58], and similar, comparable behaviors via FSCV appeared in Figure S27c.
363 Intracranial temperature is also one of key physiological parameters related to blood
364 circulation in the brain. Properties of temperature meters in animal models were evaluated
365 through tests, for example, changes in environmental conditions such as heating and cooling
366 induced a variation of temperature in the brain of animal models (Figure. 4j). Experimental
367 results indicated that measured brain temperatures from both a transient Mo RTD component
368 and standard, benchmarked temperature sensor matched fairly well. Figure 4k presents
369 obvious, immediate responses of brain temperature elicited by MFB stimulation,
370 demonstrating the capacity of the Mo-based temperature sensor for monitoring thermal
371 fluctuations in the brain.
372
373 **Evaluations on Biocompatibility of implanted electronic systems in the Brain**
374 To investigate in vivo toxicity of materials and device components of the integrated
375 brain-hacking system, we implanted resorbable probes containing MoS_2-Fe and WS_2-Fe into
376 the rat brains and examined biological responses at various stages after implantation (Figure
377 5a). Surgical procedures in detail appeared in method section. Brain tissues were
378 explanted from the rats at 1, 2, 4, and 8 weeks, histological analyses were conducted after

fixation procedures. A brain tissue at the initial step in Figure 5b, neurons around the implantation site were immediately damaged by a surgical procedure, however neighboring neurons remained intact, similar to morphology and viability of the native brain. Cross-sectional immunofluorescence images exhibit glial reactions including both Iba1 (microglia) and GFAP (reactive astrocyte) signals near locations of the implanted neural probes coated with MoS_2-Fe (Figure 5c) and WS_2-Fe (Figure S28). At the early stage (week 1), Iba-1 and GFAP signals were expressed higher around the implanted region than the sham group, but the signals tended to decline over time. Indeed, quantitative analysis presents that the Iba-1 and GFAP expression ratio values were the highest during the first week (Iba-1 expression ratio values of 43.2 ± 3.8% and 42.1 ± 5.3% in MoS_2 and WS_2, and GFAP expression ratio values of 39.4 ± 9.8% and 48.6 ± 7.5% in MoS_2 and WS_2, respectively), and then gradually decreased to approximate the values in the sham group at 8 weeks (Iba-1 expression ratio p values of 0.14 and 0.10 in MoS_2 and WS_2, and GFAP expression ratio p values of 0.03 and 0.41 in MoS_2 and WS_2 compared to the control group; Figure 5d). Taken together, the results indicate the constituent elements induced minimal effects to the immune system during the first 2 weeks postoperative period and underwent bioresorption without undesired interruption to the recovery of the brain tissue in the following period. Similar studies using a biodegradable polymer, polycaprolactone (PCL), appears in Figure S29-S31.

CONCLUSION

The concepts, materials, devices, and integration approaches reported here proposed a silicon-based biodegradable electrochemical platform for monitoring and analyzing local, temporal behaviors of neurochemicals and peripheral vital signs in deep brain regions. Materials study with theoretical calculations supported motivation of a combined use of chemically exfoliated 2D layered materials with Fe catalysts, which enhanced the

404 electrostatic force of attraction, reaction probability and charge transport, leading to
405 noticeable responses in sensitive and selective properties. A wide range of measurements
406 and analyses of devices revealed that proper selection of MoS_2 or WS_2 could provide options
407 for short- or long-term monitoring tools, further suggesting that diverse bioresorbable
408 electrochemical systems could be created through coupling with other 2D materials. The
409 results from in vivo assessments described that integration of 2D materials with soft,
410 bioresorbable electronic sensor arrays can provide potentials for envisioned uses in medically
411 useful areas.
412

Methods

Fabrication of a bioresorbable silicon-based brain-hacking system. Fabrication began with thermal growth (1100 ^{o}C, 30 min.) of 100 nm of silicon dioxide (SiO_2) as a diffusion mask for selective formation of boron-doped regions of a device layer on a silicon-on-insulator (p-type, top Si 300 nm, SOITEC, France) wafer. Modulated doping profiles for active sensing and contact regions were created by photolithography, immersion in buffered oxide etchant (BOE, J. T. Baker, USA), and subsequent high-temperature processing with spin-on-dopants (SOD, Filmtronics, USA) at 800 and 1050 ^{o}C, respectively. The top Si NM layer was released via removal of a buried oxide layer by wet etching with hydrofluoric acid (49 % HF, J. T. Baker, USA), and transferred onto a temporary carrier wafer coated with sacrificial layers of poly(methyl methacrylate) (PMMA, Microchem, USA)/polyimide (PI, Sigma-Aldrich). Photolithographic patterning and reactive ion etching (RIE) procedures configured the Si NM layer into desired geometries including ribbon-shaped transducers of dopamine sensor, resistive electrodes of pH sensors, and capacitive electrophysiology (EP) electrodes. SiO_2 layers as interlayer dielectrics were deposited by plasma-enhanced chemical vapor deposition (PECVD), and partially opened for active windows and contact pads by buffered oxide etchant (BOE, J. T. Baker, USA). A sputtered thin molybdenum (Mo) layer (thickness 100 nm) was delineated meander-shape as a temperature sensor component by photolithography and lift-off procedures in acetone. Physical deposition yielded patterned conducting traces of Mg (thickness 1 μm) as interconnects and electrodes. A thin layer of SiO_2 served as encapsulation, with openings for active windows and contact pads by BOE. Dry etching and immersion in acetone enabled transfer printing of the whole system onto any of interested flexible, biodegradable substrates. After surface modification procedures, a CO_2 laser system (VLS 3.50, Universal Laser Systems, USA) shaped the electronic brain probe and systems into configurations suitable for brain experiments.

Preparation and functionalization of 2D transition metal dichalcogenides (TMDs) nanosheets. Li intercalation was achieved by using the mixture of 25 mg of TMD powders (MoS_2, WS_2, Sigma-Aldrich) and 2.5 mL of n-BuLi in hexane (1.6 M, Sigma-Aldrich) sealed in a Teflon-lined autoclave under an argon atmosphere. The process was performed at various temperatures of 25, 75, and 130 ^oC for 48 h. The lithium-intercalated products (Li_xMoS_2, Li_xWS_2) were then washed 3 times with anhydrous hexane and added into 25 mL of aqueous solution (35 mM) of mercaptopropionic acid (MPA, Alfa Aesar, USA). Ultrasonication of the mixture for 1 h resulted in exfoliation of TMD nanosheets functionalized with the carboxyl group (-COOH). Non-exfoliated large flakes were removed by centrifugation at 3000 rpm for 10 min, and further purified by dialysis with 100-500 D membranes (Spectrum Labs, USA) for 5 days. Finally, the dispersed TMD nanosheets were added to various concentrations (0.1 mM, 1 mM, 5 mM, 10 mM) of an iron precursor ($FeCl_3$), followed by an addition of reductant ($NaBH_4$) of 15 mM with subsequent ultrasonication for 1 h to decorate Fe-NP catalysts to active sites of TMDs.

Evaluation on dissolution kinetics. Physical, chemical, and structural measurements were exploited to study time-dependent degradations of MoS_2 and WS_2 in phosphate-buffed saline (PBS) and artificial cerebrospinal fluid (ACSF) at body temperature (37 ^oC). Investigations of changes in chemical compositions using ion chromatography (IC), and structural and optical properties using Raman spectroscopy verified dissolution behaviors of MoS_2 and WS_2.

Evaluation in animal models. All surgical experiments were performed on anesthetized rats according to ethical standards and methods approved by Institutional Animal Care and Use Committee. Sprague-Dawley rats (12-14 weeks, 300-350 g, male, Koatech, Korea)

were anesthetized using 14 wt% of urethane solution with the amount of 8 mg/kg and stabilized in a commercially available stereotaxic frame (David Kopf Instruments, Tujunga, CA) at 37 ^{o}C for the duration of the surgical procedure and measurements. Craniotomy was performed three individual holes with the diameter of 1.5 mm in the skull for the implantation of electrodes including recording probes, a bipolar electrical stimulating electrode and Ag/AgCl reference electrode. The recording probe consist of three parts: carbon fiber microelectrode (CFM) as a guiding electrode, the bioresorbable probe and a custom-made stereotactic frame. Recording probes were injected to the dorsal striatum at the right hemisphere as stereotactic coordinates: (Anterior-Posterior +1.2 mm, Medial-Lateral +2.0 mm, Dorsal-Ventral -4.5 mm). A commercial bipolar stainless-steel electrophysiology electrode (Plastic One, MS303/2, Roanoke, VA, USA) was inserted to ipsilateral medial forebrain bundle (MFB) as stereotactic coordinates: (Anterior-Posterior -4.6 mm, Medial-Lateral +1.4 mm, Dorsal-Ventral -8.0 mm). Ag/AgCl reference electrodes were prepared from Ag microwire (A-M systems, USA) soaked in sodium hypochlorite solution (Sigma-Aldrich, 4.00 – 4.99 %) for 10 min, and positioned superficially in cortical tissue contralateral to the recording probes and stimulating electrode. Custom-made stereotactic frame composed of biodegradable plastics (polylactic acid (PLA)) was created with a customized design for the soft neural probes using a DIY 3D printer (Creality 3D, China). The craniectomy voids were enclosed by ultraviolet curable epoxy glue and bone wax, and the electronic wireless system was placed on the outside surface of the skull. Epicranial incision closure was performed by interrupted sutures utilizing bioabsorbable threads.

In vivo recordings of evoked responses by electrical stimulation. A customized electronic platform was used to perform FSCV and electrical stimulation to identify dopamine releasing sites in the dorsomedial striatum. In all cases of FSCV, the potential

sweep was performed at a frequency of 10 Hz with a scan rate of 400 V/s in the voltage range of -0.4 to 1.3 V. A train of bipolar pulses (2 ms pulse width, 200 μA, 60 Hz) was delivered for 3 seconds to identify dopamine releasing sites in the striatum. The measured neural responses in the brain sensor arrays were recorded by wireless communications through biofluids and tissues with rates of up to 10 Hz. Custom LabVIEW software (National Instruments) controls the electrical systems and acquired electrically measured data.

In vivo examinations in biocompatibility of neural probes. All animal experiments were conducted in accordance with the ethical guidelines and the standard operating protocols of the Institutional Animal Care and Use Committee (IACUC). Sprague-Drawly rats (12-week-old, male, Koatech, Korea) implanted with brain probes (built with each TMD on PLGA and PCL substrates, respectively) were classified as an implantation period of 1 week, 2 weeks, 4 weeks, and 8 weeks (n = 3 for each group). The rats were anesthetized using inhalation anesthesia systems (isoflurane 2-5 % with O_2 1 L/min) and fixed with intracardiac perfusions using 4 % paraformaldehyde in phosphate buffer saline (PBS) solutions. Then, the brains were gently extracted and post-fixed for 24 h at 4 ^{o}C. For histological evaluation, the explanted brain tissues were embedded in optimal cutting temperature compound (OCT; Leica, Germany) and sectioned at a thickness of 20 μm by using a cryomicrotome (HM525 NX; Thermo Fisher Scientific, Waltham, MA, USA). Brain sections were then fixed with cold fixative for 30 min and washed with PBS. The sections were permeabilized with 0.3 vol% Triton X-100 in PBS, blocked with 4 vol% bovine serum albumin (BSA; Sigma aldrich, Saint Louis, MO, USA) in PBS at room temperature, and incubated initially with primary antibodies at 4 ^{o}C overnight. Secondary antibodies were treated for 2 h and mounted with Vectashield mounting medium with 4,6-diamidino-2-phenylindole (DAPI) (Vector Labs, CA, USA). Images were obtained using a confocal laser scanning microscope (LSM700; Carl

Zeiss, Oberkochen, Germany). To estimate the microglia/macrophages reaction and astrogliosis in the vicinity of the implants, the primary antibodies were rabbit monoclonal anti-ionized calcium-binding adapter molecule 1 (Iba-1 at 1:500; Abcam, Cambridge, England) and mouse polyclonal anti-glial fibrillary acidic protein (GFAP at 1:1000; Sigma). The Iba-1 and GFAP-positive areas in five random fields (×200 magnification) were quantified using Image J software (n = 3 in each group).

Acknowledgements

This work supported by a Korea University grant, KU-KIST Graduate School of Converging Science and Technology Program, National Research Foundation of Korea (NRF) grant funded by the Korea government (MSIT) (grant NRF-2017R1E1A1A01075027, NRF-2017R1A2B2006896, and NRF-2020R1A2C2009389), and the Technology In-novation Program (20002974, development of biosensing function antibiosis wound dressing and instrument for the treatment) funded by the Ministry of Trade, Industry & Energy (MOTIE, Korea). Computations for this research were performed on the Pennsylvania State University's Institute for Computational and Data Sciences Advanced CyberInfrastructure (ICDS-ACI). H.C. also acknowledges the support from the Doctoral New Investigator grant from the American Chemical Society Petroleum Research Fund (59021-DNI7) and National Science Foundation (ECCS-1933072).

Author Contributions

S.M.Y., T.-M.J., G.-J.K., J.C.C., J.-W.S., J.H.L., and S.-W.H. accomplished designing and fabricating the sensors and electronics. J.H.S., Y.S.K., S.-Y.J., and C.-H.L. synthesized and analyzed the materials. H.-U.C., J.S., Y.M.K., and D.P.J. performed the animal experiments. T.H.K., S.P., and Y.J. analyzed the immunohistochemistry. J.Z. and H.C. accomplished the computational simulations.

Competing interest

The authors declare no competing interest.

References

1. Thakor, N. V. & Tong, S. Advances in quantitative electroencephalogram analysis methods. *Annu. Rev. Biomed. Eng.* **6**, 453–495 (2004).

2. Goldberger, A. L., Goldberger, Z. D. & Shvilkin, A. *Goldberger's Clinical Electrocardiography*. (Elsevier, 2018).

3. Grady, M., Pineau, M., Pynes, M. K., Katz, L. B. & Ginsberg, B. A clinical evaluation of routine blood sampling practices in patients with diabetes: Impact on fingerstick blood volume and pain. *J. Diabetes Sci. Technol.* **8**, 691–698 (2014).

4. DeWitt, D. E. & Hirsch, I. B. Outpatient Insulin Therapy in Type 1 and Type 2 Diabetes Mellitus: Scientific Review. *J. Am. Med. Assoc.* **289**, 2254–2264 (2003).

5. Dykstra, A. R. *et al.* Individualized localization and cortical surface-based registration of intracranial electrodes. *Neuroimage* **59**, 3563–3570 (2012).

6. Maynard, E. M., Nordhausen, C. T. & Normann, R. A. The Utah Intracortical Electrode Array: A recording structure for potential brain-computer interfaces. *Electroencephalogr. Clin. Neurophysiol.* **102**, 228–239 (1997).

7. Kringelbach, M. L., Jenkinson, N., Owen, S. L. F. & Aziz, T. Z. Translational principles of deep brain stimulation. *Nat. Rev. Neurosci.* **8**, 623–635 (2007).

8. Serruys, P. W. *et al.* A Comparison of Balloon-Expandable-Stent Implantation with Balloon Angioplasty in Patients with Coronary Artery Disease. *N. Engl. J. Med.* **331**, 489–495 (1994).

9. Tang, A. S. L. *et al.* Cardiac-Resynchronization Therapy for Mild-to-Moderate Heart Failure. *N. Engl. J. Med.* **363**, 2385–2395 (2010).

10. Kim, D. H. *et al.* Epidermal electronics. *Science* **333**, 838–843 (2011).

11. Wang, S. *et al.* Skin electronics from scalable fabrication of an intrinsically stretchable transistor array. *Nature* **555**, 83–88 (2018).

12. Yu, X. *et al.* Skin-integrated wireless haptic interfaces for virtual and augmented reality. *Nature* **575**, 473–479 (2019).

13. Chung, H. U. *et al.* Binodal, wireless epidermal electronic systems with in-sensor analytics for neonatal intensive care. *Science* **363**, 0–13 (2019).

14. Miyamoto, A. *et al.* Inflammation-free, gas-permeable, lightweight, stretchable on-skin electronics with nanomeshes. *Nat. Nanotechnol.* **12**, 907–913 (2017).

15. Oh, J. Y. *et al.* Intrinsically stretchable and healable semiconducting polymer for organic transistors. *Nature* **539**, 411–415 (2016).

16. Son, D. *et al.* An integrated self-healable electronic skin system fabricated via dynamic reconstruction of a nanostructured conducting network. *Nat. Nanotechnol.* **13**, 1057–1065 (2018).

17. Kim, T. Il *et al.* Injectable, cellular-scale optoelectronics with applications for wireless optogenetics. *Science* **340**, 211–216 (2013).

18. Mickle, A. D. *et al.* A wireless closed-loop system for optogenetic peripheral neuromodulation. *Nature* **565**, 361–365 (2019).

19. Jeong, J. W. *et al.* Wireless Optofluidic Systems for Programmable In Vivo Pharmacology and Optogenetics. *Cell* **162**, 662–674 (2015).

20. Lee, H. *et al.* A graphene-based electrochemical device with thermoresponsive microneedles for diabetes monitoring and therapy. *Nat. Nanotechnol.* **11**, 566–572 (2016).

21. Minev, I. R. *et al.* Electronic dura mater for long-term multimodal neural interfaces. *Science* **347**, 159–163 (2015).

22. Hwang, S.-W. *et al.* A Physically Transient Form of Silicon Electronics. *Science* **337**, 1640–1644 (2012).

23. Kang, S. *et al.* Bioresorbable silicon electronic sensors for the brain. *Nature* **530**, 71–76 (2016).

24. Yu, K. J. *et al.* Bioresorbable silicon electronics for transient spatiotemporal mapping of electrical activity from the cerebral cortex. *Nat. Mater.* **15**, 782–91 (2016).

25. Koo, J. *et al.* Wireless bioresorbable electronic system enables sustained nonpharmacological neuroregenerative therapy. *Nat. Med.* **24**, 1830–1836 (2018).

26. Krishnan, S. R. *et al.* Epidermal electronics for noninvasive, wireless, quantitative

assessment of ventricular shunt function in patients with hydrocephalus. *Sci. Transl. Med.* **10**, (2018).

27. Dagdeviren, C. *et al.* Conformal piezoelectric systems for clinical and experimental characterization of soft tissue biomechanics. *Nat. Mater.* **14**, 728–736 (2015).

28. Choi, S. *et al.* Highly conductive, stretchable and biocompatible Ag–Au core–sheath nanowire composite for wearable and implantable bioelectronics. *Nature Nanotechnology* **13**, 1048–1056 (2018).

29. Gao, W. *et al.* Fully integrated wearable sensor arrays for multiplexed in situ perspiration analysis. *Nature* **529**, 509–514 (2016).

30. Frank, J. A., Antonini, M. J. & Anikeeva, P. Next-generation interfaces for studying neural function. *Nat. Biotechnol.* **37**, 1013–1023 (2019).

31. Clark, J. J. *et al.* Chronic microsensors for longitudinal, subsecond dopamine detection in behaving animals. *Nat. Methods* **7**, 126–129 (2010).

32. Akinwande, D., Petrone, N. & Hone, J. Two-dimensional flexible nanoelectronics. *Nat. Commun.* **5**, 5678 (2014).

33. Huang, Y. C. *et al.* Sensitive pressure sensors based on conductive microstructured air-gap gates and two-dimensional semiconductor transistors. *Nat. Electron.* **3**, 59–69 (2020).

34. Lin, Z. *et al.* Solution-processable 2D semiconductors for high-performance large-area electronics. *Nature* **562**, 254–258 (2018).

35. McManus, D. *et al.* Water-based and biocompatible 2D crystal inks for all-inkjet-printed heterostructures. *Nat. Nanotechnol.* **12**, 343–350 (2017).

36. Radisavljevic, B., Radenovic, A., Brivio, J., Giacometti, V. & Kis, A. Single-layer MoS_2 transistors. *Nat. Nanotechnol.* **6**, 147–150 (2011).

37. Britnell, L. *et al.* Strong Light-Matter Interactions in Heterostructures of Atomically Thin Films. *Science* **340**, 1311–1314 (2013).

38. Lee, C. H. *et al.* Atomically thin p-n junctions with van der Waals heterointerfaces. *Nat. Nanotechnol.* **9**, 676–681 (2014).

39. Jariwala, D., Marks, T. J. & Hersam, M. C. Mixed-dimensional van der Waals heterostructures. *Nat. Mater.* **16**, 170–181 (2017).

40. Amani, M. *et al.* Near-unity photoluminescence quantum yield in MoS_2. *Science* **350**, 1065–1068 (2015).

41. Jaramillo, T. F. *et al.* Identification of active edge sites for electrochemical H_2 evolution from MoS_2 nanocatalysts. *Science* **317**, 100–102 (2007).

42. Voiry, D. *et al.* Enhanced catalytic activity in strained chemically exfoliated WS_2 nanosheets for hydrogen evolution. *Nat. Mater.* **12**, 850–855 (2013).

43. Coleman, J. N. *et al.* Two-dimensional nanosheets produced by liquid exfoliation of layered materials. *Science* **331**, 568–571 (2011).

44. Chhowalla, M. *et al.* The chemistry of two-dimensional layered transition metal

dichalcogenide nanosheets. *Nat. Chem.* **5**, 263–275 (2013).

45. Voiry, D. *et al.* Covalent functionalization of monolayered transition metal dichalcogenides by phase engineering. *Nat. Chem.* **7**, 45–49 (2015).

46. Kappera, R. *et al.* Phase-engineered low-resistance contacts for ultrathin MoS_2 transistors. *Nat. Mater.* **13**, 1128–1134 (2014).

47. Acerce, M., Voiry, D. & Chhowalla, M. Metallic 1T phase MoS_2 nanosheets as supercapacitor electrode materials. *Nat. Nanotechnol.* **10**, 313–318 (2015).

48. Yu, Y. *et al.* High phase-purity 1T′-MoS_2- and 1T′-$MoSe_2$-layered crystals. *Nat. Chem.* **10**, 638–643 (2018).

49. Aitken, P. G. *et al.* Preparative methods for brain slices: a discussion. *J. Neurosci. Methods* **59**, 139–149 (1995).

50. Guo, Y., Liu, D. & Robertson, J. Chalcogen vacancies in monolayer transition metal dichalcogenides and Fermi level pinning at contacts. *Appl. Phys. Lett.* **106**, 173106 (2015).

51. Duerloo, K. A. N., Li, Y. & Reed, E. J. Structural phase transitions in two-dimensional Mo-and W-dichalcogenide monolayers. *Nat. Commun.* **5**, (2014).

52. Chou, S. S. *et al.* Ligand conjugation of chemically exfoliated MoS_2. *J. Am. Chem. Soc.* **135**, 4584–4587 (2013).

53. Yang, F., Liu, Y., Gao, L. & Sun, J. pH-sensitive highly dispersed reduced graphene oxide solution using lysozyme via an in situ reduction method. *J. Phys. Chem. C* **114**, 22085–22091 (2010).

54. Chen, X. *et al.* CVD-grown monolayer MoS_2 in bioabsorbable electronics and biosensors. *Nat. Commun.* **9**, (2018).

55. Chen, S. M. & Peng, K. T. The electrochemical properties of dopamine, epinephrine, norepinephrine, and their electrocatalytic reactions on cobalt(II) hexacyanoferrate films. *J. Electroanal. Chem.* **547**, 179–189 (2003).

56. Holmwood, R. A. & Glang, R. Resistivity and Temperature Coefficient of Pure Molybdenum. *J. Chem. Eng. Data* **10**, 162–163 (1965).

57. John, C. E., Budygin, E. A., Mateo, Y. & Jones, S. R. Neurochemical characterization of the release and uptake of dopamine in ventral tegmental area and serotonin in substantia nigra of the mouse. *J. Neurochem.* **96**, 267–282 (2006).

58. Heien, M. L. A. V. *et al.* Real-time measurement of dopamine fluctuations after cocaine in the brain of behaving rats. *Proc. Natl. Acad. Sci. U. S. A.* **102**, 10023–10028 (2005).

675 **Figure Captions**

676

677 **Figure 1. Soft, bioresorbable silicon-based brain-hacking probes with arrays of**
678 **electronic sensors for neurochemicals and neurophysiologies in the deep brain.** (a)
679 Schematic illustration of a biodegradable, implantable electrochemical brain-hacking system
680 for investigating neurotransmitters with associated variations in pH, temperature, and
681 electrophysiological signals. Key components in active sensing regions for neurochemicals
682 were composed of a combination of heterogeneous single-crystal silicon nanoribbons (Si NRs)
683 as an electrode, iron nanoparticles (Fe NPs) for a catalyst, and two-dimensional (2D)
684 transition metal dichalcogenides (TMD) nanosheets (MoS_2, WS_2) for charge transfer and
685 electrostatic attraction. (b) A representative image of the neural probe at a deformed state
686 with a conventional syringe needle (D, ~1 mm) for comparison of the actual size, with a
687 magnified view in the inset. (c) Underlying electrochemical mechanism of the brain-
688 hacking system responsive to neurotransmitters. Cationic dopamine (DA) was strongly
689 attracted to negatively charged TMD surfaces and converted to dopamine quinone (DQ)
690 through catalytic oxidations by the Fe NPs decorated on the TMDs, producing electrons
691 passing through the 1T metallic TMDs to the Si NM transducers. (d) A series of dissolution
692 images of chemically exfoliated TMDs (top, MoS_2; bottom, WS_2) during immersion in a
693 phosphate buffer saline (PBS) solution with expedited mode (pH 11) at room temperature.

694

695 **Figure 2. Design, synthesis, and characterizations of 0D-2D hetero-structured**
696 **nanomaterials for bioresorbable electrochemical systems.** (a) Representative
697 transmission electron microscopy (TEM) images of the 1T TMDs decorated with Fe NPs.
698 (b) Evolutions of Raman spectra of chemically exfoliated, carboxyl-functionalized MoS_2 and
699 WS_2 with lithium intercalation at various temperatures. As the reaction temperature

700 increased, features associated with the 1T-MoS_2 and -WS_2 became dominant, while 2H-phase
701 characteristics of the both materials relatively faded away. (c) Temperature-dependent phase
702 transition of the Li-intercalated MoS_2 analyzed by x-ray photoemission spectroscopy (XPS),
703 indicating gradual increase of 1T-relevant properties. (d) Summarized results in the 1T
704 fractions and atomic ratio depending on exfoliation temperature conditions of TMDs. (e)
705 Negative electrostatic potentials of engineered TMDs, Fe NPs-coupled TMDs nanosheets and
706 control groups. (f, g) Determination of catalytic dopamine oxidations with the assembled
707 materials using high-performance liquid chromatography (HPLC). Chromatograms as a
708 function of obtained times with magnified plots at the interested detection times (1.7 min) in
709 the insets. (h) Normalized peak areas from the chromatograms as amount of output
710 products through dopamine oxidation at different collection periods. (i) Comparison of
711 measured cyclic voltammograms revealing enhanced electrochemical dopamine reactions
712 with addition of the hybrid nanomaterials. (j, k) Charge density and distance between
713 dopamine and individual materials (j) (left, 2H MoS_2; right, 2H MoS_2-Fe) and (k) (left, 1T
714 MoS_2; right, 1T MoS_2-Fe). Red and blue denote the gain and loss of electrons, respectively.
715 (l) Calculated adsorption energy of DA molecules for the respective elements. (m)
716 Description of chemical dissolution process of TMDs via hydrolysis. (n) Observations of
717 gradual increases of SO_4^{2-} as a byproduct using ion chromatography during dissolution of
718 TMDs in PBS (0.1 M, left) and ACSF (1X, right) at body temperature (37 ^{o}C), respectively.
719 (o) Summarized amounts of decomposed TMDs in biological buffer solutions.
720
721 **Figure 3. Electrochemical and electronic properties of brain-hacking probes.** (a)
722 Electrochemical properties of MoS_2-Fe- (red) and WS_2-Fe-coated (blue) Si NR electrodes in
723 an extensive range of dopamine concentrations. The dotted line indicates limit-of-detection
724 (LOD). (b) Measured fractional current ratio of the MoS_2-Fe- (red), WS_2-Fe- (blue) coated,

and pristine Si NR (black, X10 signal) electrodes to various extents of dopamine amounts over time, detectable up to a femtomolar (fM, 10^{-15}) concentration. (c) Measurements through over 120 repeated reactions with alternating immersions in DA (1 pM) and DA-free (PBS) solutions. (d) Comparison of normalized responses of modified, functionalized Si NR electrodes (MoS_2-Fe- (black), WS_2-Fe- (red) coated Si NR, and hydroxy-terminated Si NR electrodes (blue)), showing highly selective responses of TMD-Fe-coated Si NR electrodes to dopamine over diverse neurotransmitters involving epinephrine (EP), norepinephrine (NE), serotonin (5-HT), uric acid (UA), and ascorbic acid (AA). (e) Temporal, continuous electrical behaviors indicating excellent selectivity of the MoS_2-Fe-coated devices to dopamine among the previous chemical in (d). (f) Electrical behaviors of amino-functionalized Si NR-based pH meters over a wide range of pH values. (g) Temperature-dependent changes in resistance of dissolvable molybdenum (Mo)-based temperature detectors. (h) Real-time responses of the transient Mo temperature detectors, consistent with measured values from a commercial, standard thermometer under a temperature-variant environment. (i) Measurements of electrochemical impedances of electrophysiological (EP) electrodes, magnitudes (left) and phases (right) corresponding to each frequency.

Figure 4. In vivo evaluations of biodegradable electronic neurochemical analyzers. (a) Schematic illustrations of targeted dopaminergic pathway and corresponding locations of stimulation and recording electrodes. The nigrostriatal pathway, the dopaminergic pathway of interest, links the substantia nigra pars compacta (SNc) in the midbrain with the dorsal striatum (STr) in the forebrain. (b) Neural probes positioned at the dorsal striatum with a carbon fiber microelectrode (CFM) as a guide for addressing recording sites and confirmation of dopamine signal. (c) Spatiotemporal dopamine (DA) responses evoked by stimulations,

recorded by bioresorbable electrochemical neural probes. (d) Summarized instantaneous DA responses obtained as current changes in the bioresorbable DA components. The gray shading indicates a measure of error (n = 6, biologically independent rats). (e) A representative colored plot from a carbon microfiber electrode, verifying that temporal current changes at +0.2 V/-0.3 V corresponding to the oxidation/reduction potential of DA were closely related to DA releases induced by electrical stimulations. (f) Phasic DA responses from the oxidation current changes at +0.2 V in FSCV, similar to that in (d). (g) Real-time, continuous responses of resorbable neurochemical probes over a long range of timeframes, with intermittent electrical stimulations and nomifensine as a DA reuptake inhibitor. (h) Normalized amplitudes and durations of the DA signals, before/after injection of nomifensine. (i) Temporary pH fluctuation in local areas of the brain associated with the DA release. (j) Recordings of relevant temperature variations using the integrated bioresorbable probes in response to external temperature conditions, with plots of a commercial product. (k) Observation of local brain temperatures accompanied with the release of DA by electrical stimulations.

Figure 5. In vivo toxicity of dissolvable neural probes. (a) A photograph of an extracted rat brain one week after implantation, with a magnified view of the inserted site in the inset. (b) Nissl-stained image of a thin, horizontal piece of brain tissues at first week post-surgery. (c) Diverse sets of cross-sectional fluorescence profiles of device-implanted sites examined at different stages after surgical interventions, with immunofluorescent (IF) staining for activated microglia (green, ionized calcium binding adaptor molecule (Iba-1)), astrocytes (red, glial fibrillary acidic protein (GFAP)), and nuclei (blue, 4′,6-diamidino-2-phenylindole (DAPI)). (d) Quantitative evaluations of inflammatory glial responses (left, microglia cells;

774 right, astrocytes) to the implanted, dissolvable neural probes, indicating no significant
775 differences in the immune responses 8 weeks after implantation compared to values of the
776 sham group.
777

a

Microcontroller
Interconnects
Dielectrics
RF coil
Substrates

Wireless Communication System

Biodegradable Soft Neural Probe & System

Bioresorbable Neural Probe

Encapsulation
Temperature sensor
Interlayer dielectrics
pH sensor
EP sensor
Dopamine sensor
Polymer needle

Biodegradable Electrochemical System

Catalyst NPs
2D TMDs
Si NMs

Human Brain

b

Electronic components for NFC
Brain tissue phantom
Sensor arrays
1 mm
T sensor
pH sensor
EP sensor
Dopamine sensor
Mg coil & interconnects
Inserted biodegradable soft neural probe
10 mm

c

Electrostatic attraction
Dopamine
Dopamine quinone
Catalytic Oxidation
Electrostatic Potential
(iii) Fe NPs
(ii) 1T TMDs
(i) p-doped Si NMs
Electron transfer

d

PBS (pH 11 @ 60 °C) Initial
1 hour
5 hours
2 day
MoS2
Fully dissolved
WS2
PBS (pH 11 @ 60 °C) Initial
1 day
4 day
7 day

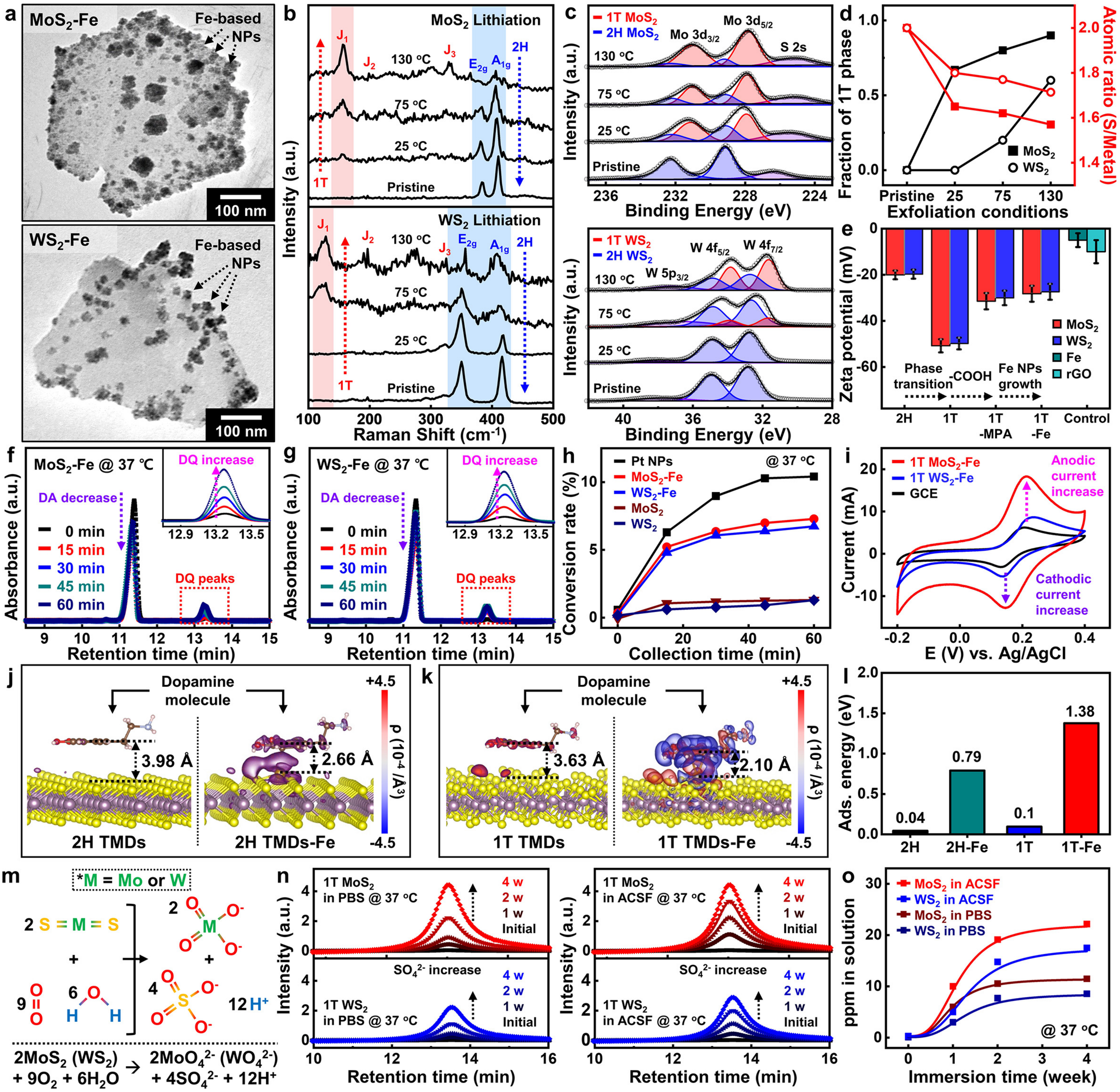
a
MoS2-Fe
Fe-based NPs
100 nm
WS2-Fe
Fe-based NPs
100 nm
b
MoS2 Lithiation
J1
J2
J3
E2g
A1g
2H
1T
130 °C
75 °C
25 °C
Pristine
WS2 Lithiation
Intensity (a.u.)
Raman Shift (cm-1)
c
1T MoS2
2H MoS2
Mo 3d3/2
Mo 3d5/2
S 2s
130 °C
75 °C
25 °C
Pristine
Intensity (a.u.)
Binding Energy (eV)
1T WS2
2H WS2
W 4f5/2
W 4f7/2
W 5p3/2
d
Fraction of 1T phase
Atomic ratio (S/Metal)
MoS2
WS2
Pristine
25
75
130
Exfoliation conditions
e
Zeta potential (mV)
MoS2
WS2
Fe
rGO
Phase transition
-COOH
Fe NPs growth
2H
1T
1T -MPA
1T -Fe
Control
f
MoS2-Fe @ 37 °C
DQ increase
DA decrease
0 min
15 min
30 min
45 min
60 min
DQ peaks
Absorbance (a.u.)
Retention time (min)
g
WS2-Fe @ 37 °C
DQ increase
DA decrease
0 min
15 min
30 min
45 min
60 min
DQ peaks
Absorbance (a.u.)
Retention time (min)
h
Pt NPs
MoS2-Fe
WS2-Fe
MoS2
WS2
@ 37 °C
Conversion rate (%)
Collection time (min)
i
1T MoS2-Fe
1T WS2-Fe
GCE
Anodic current increase
Cathodic current increase
Current (mA)
E (V) vs. Ag/AgCl
j
Dopamine molecule
3.98 Å
2.66 Å
2H TMDs
2H TMDs-Fe
ρ (10-4 /Å3)
k
Dopamine molecule
3.63 Å
2.10 Å
1T TMDs
1T TMDs-Fe
ρ (10-4 /Å3)
l
Ads. energy (eV)
0.04
0.79
0.1
1.38
2H
2H-Fe
1T
1T-Fe
m
*M = Mo or W
2 S = M = S
9 O2
6 H2O
4 SO4 2-
12 H+
2MoS2 (WS2) + 9O2 + 6H2O → 2MoO4 2- (WO4 2-) + 4SO4 2- + 12H+
n
1T MoS2 in PBS @ 37 °C
1T WS2 in PBS @ 37 °C
1T MoS2 in ACSF @ 37 °C
1T WS2 in ACSF @ 37 °C
4 w
2 w
1 w
Initial
SO4 2- increase
Intensity (a.u.)
Retention time (min)
o
MoS2 in ACSF
WS2 in ACSF
MoS2 in PBS
WS2 in PBS
@ 37 °C
ppm in solution
Immersion time (week)

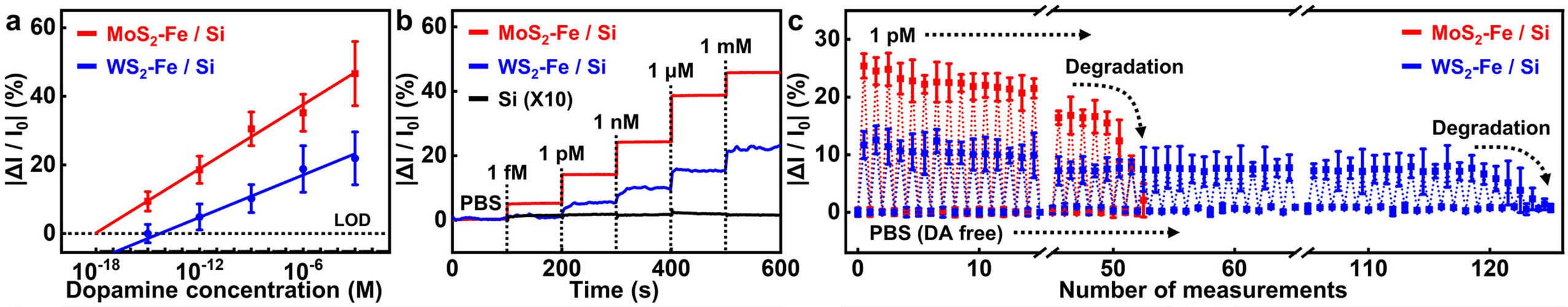
a
MoS2-Fe / Si
WS2-Fe / Si
|ΔI / I0| (%)
LOD
Dopamine concentration (M)
b
MoS2-Fe / Si
WS2-Fe / Si
Si (X10)
PBS
1 fM
1 pM
1 nM
1 μM
1 mM
Time (s)
c
1 pM
Degradation
Degradation
PBS (DA free)
MoS2-Fe / Si
WS2-Fe / Si
Number of measurements
d
MoS2-Fe / Si
WS2-Fe / Si
Si-OH
Norm. response
Dopamine
Uric acid
Ascorbic acid
Serotonin
Epinephrine
Norepinephrine
e
MoS2-Fe / Si
@ 1 nM
~ 5X signal
DA
PBS
UA
AA
5-HT
EP
NE
Time (s)
f
pH 3
pH 5
pH 7
pH 9
pH 11
Δ G (μS)
Time (s)
g
Temperature resistivity coefficient (α) = 0.0026
R² = 0.97119
Experimented
Calculated
Temperature (°C)
h
Heating up
Cooling-down
Transient sensor
Commercial sensor
Temperature (°C)
Time (min)
i
Electrode 1
Electrode 2
Electrode 3
Electrode 4
in PBS (@ 37 °C)
Log [Z] (Ω)
Frequency (Hz)
- phase (°)
Frequency (Hz)

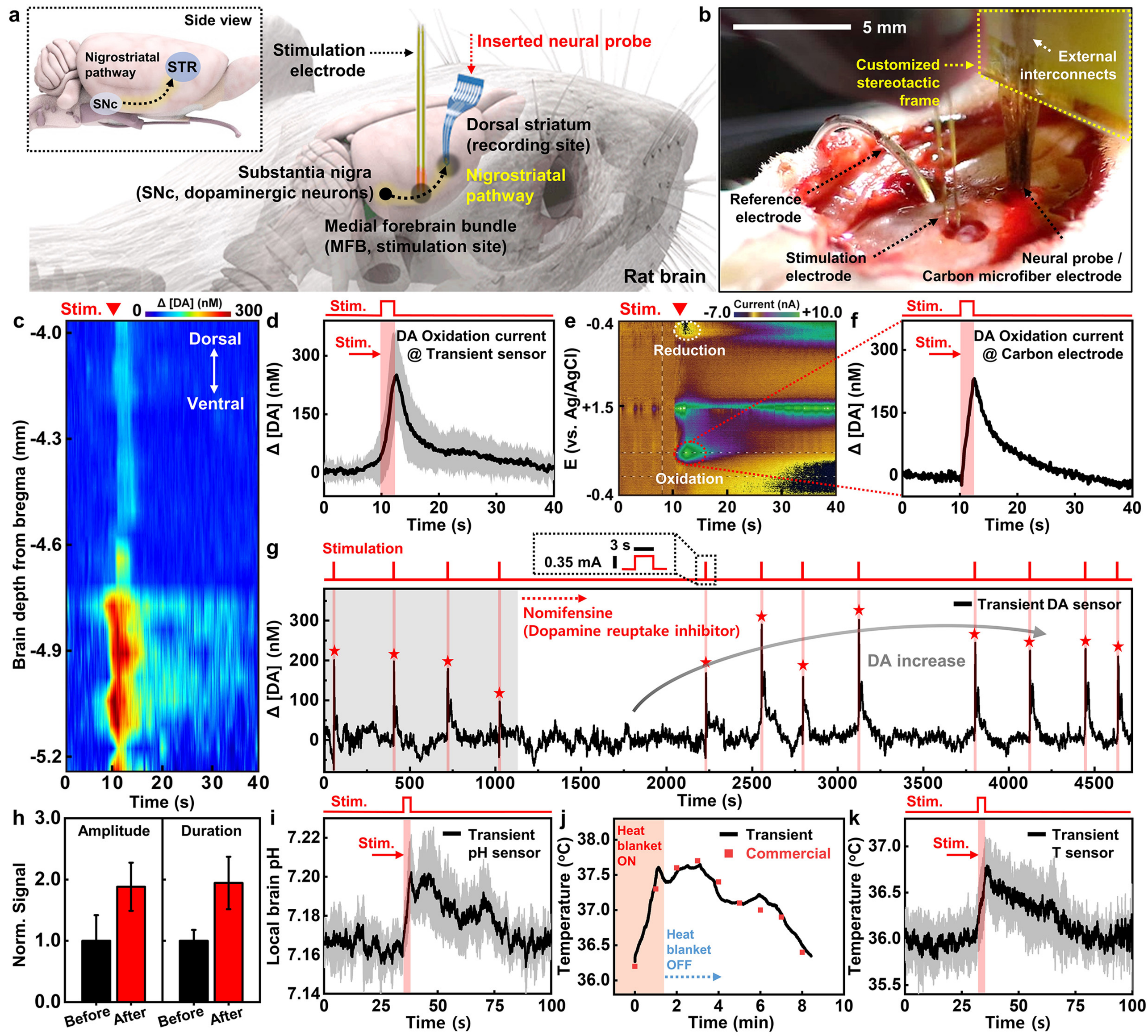
a
Side view
Nigrostriatal pathway
STR
SNc
Stimulation electrode
Inserted neural probe
Dorsal striatum (recording site)
Substantia nigra (SNc, dopaminergic neurons)
Nigrostriatal pathway
Medial forebrain bundle (MFB, stimulation site)
Rat brain
b
5 mm
Customized stereotactic frame
External interconnects
Reference electrode
Stimulation electrode
Neural probe / Carbon microfiber electrode
c
Stim.
Δ [DA] (nM)
0
300
Dorsal
Ventral
Brain depth from bregma (mm)
-4.0
-4.3
-4.6
-4.9
-5.2
Time (s)
d
Stim.
DA Oxidation current @ Transient sensor
Δ [DA] (nM)
Time (s)
e
Stim.
Current (nA)
-7.0
+10.0
Reduction
Oxidation
E (vs. Ag/AgCl)
-0.4
+1.5
-0.4
Time (s)
f
Stim.
DA Oxidation current @ Carbon electrode
Δ [DA] (nM)
Time (s)
g
Stimulation
3 s
0.35 mA
Nomifensine (Dopamine reuptake inhibitor)
Transient DA sensor
DA increase
Δ [DA] (nM)
Time (s)
h
Amplitude
Duration
Norm. Signal
Before
After
Before
After
i
Stim.
Transient pH sensor
Local brain pH
Time (s)
j
Heat blanket ON
Transient
Commercial
Heat blanket OFF
Temperature (°C)
Time (min)
k
Stim.
Transient T sensor
Temperature (°C)
Time (s)

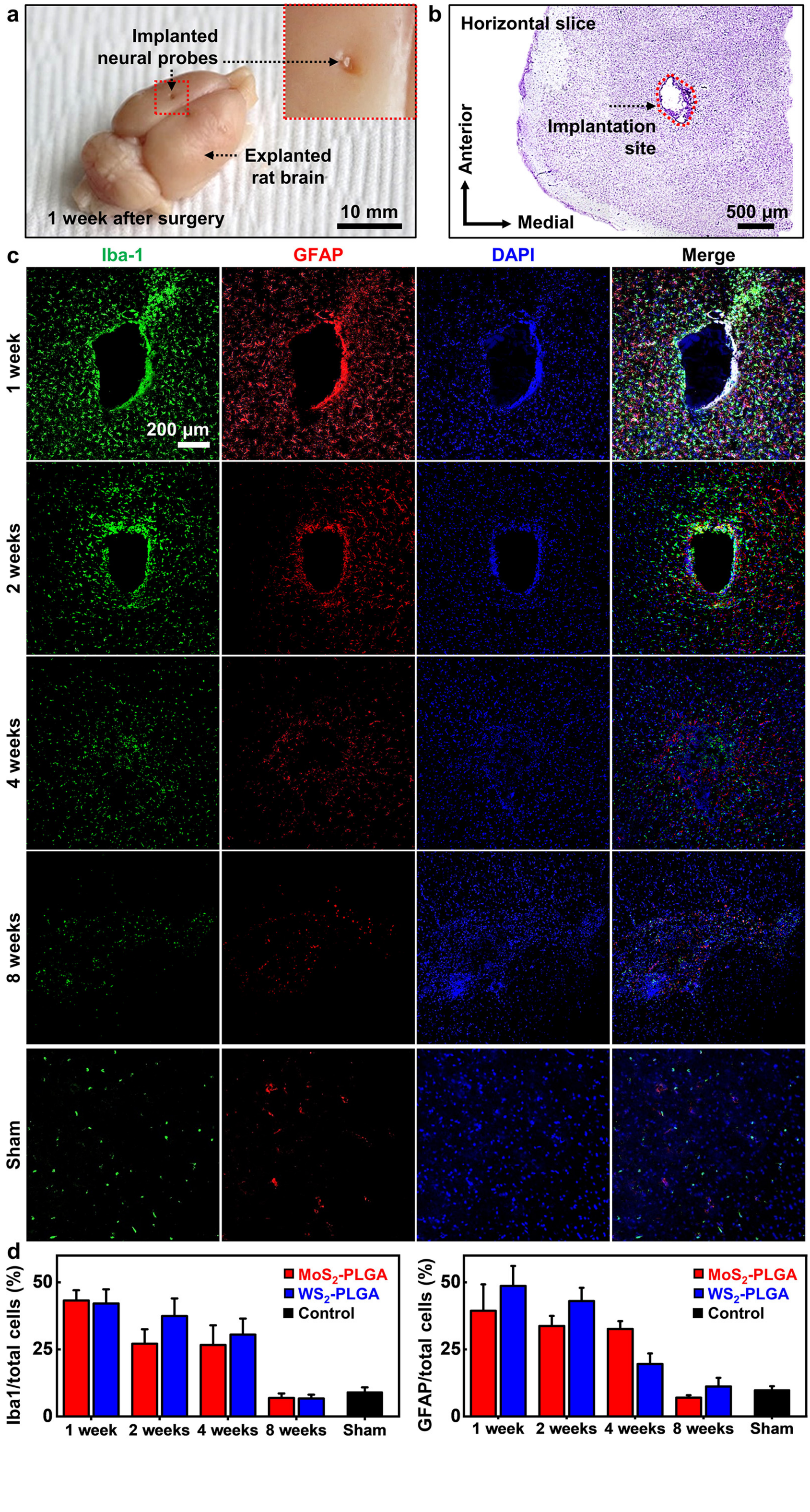
a
Implanted
neural probes
Explanted
rat brain
1 week after surgery
10 mm
b
Horizontal slice
Anterior
Medial
Implantation
site
500 μm
c
Iba-1
GFAP
DAPI
Merge
1 week
2 weeks
4 weeks
8 weeks
Sham
200 μm
d
Iba1/total cells (%)
GFAP/total cells (%)
MoS2-PLGA
WS2-PLGA
Control
50
25
0
1 week
2 weeks
4 weeks
8 weeks
Sham